

Central Lancashire Online Knowledge (CLoK)

Title	Multiphysics performance assessment of hydrogen fuelled engines
Type	Article
URL	https://clock.uclan.ac.uk/47610/
DOI	https://doi.org/10.1177/14680874231182211
Date	2023
Citation	Rahmani, Ramin, Dolatabadi, Nader and Rahnejat, Homer (2023) Multiphysics performance assessment of hydrogen fuelled engines. International Journal of Engine Research. ISSN 1468-0874
Creators	Rahmani, Ramin, Dolatabadi, Nader and Rahnejat, Homer

It is advisable to refer to the publisher's version if you intend to cite from the work.
<https://doi.org/10.1177/14680874231182211>

For information about Research at UCLan please go to <http://www.uclan.ac.uk/research/>

All outputs in CLoK are protected by Intellectual Property Rights law, including Copyright law. Copyright, IPR and Moral Rights for the works on this site are retained by the individual authors and/or other copyright owners. Terms and conditions for use of this material are defined in the <http://clock.uclan.ac.uk/policies/>

Multiphysics performance assessment of hydrogen fuelled engines

Ramin Rahmani¹ , Nader Dolatabadi¹ and Homer Rahnejat^{1,2}

International J of Engine Research
1–21

© IMechE 2023



Article reuse guidelines:

sagepub.com/journals-permissions

DOI: 10.1177/14680874231182211

journals.sagepub.com/home/ijer



Abstract

In the quest for decarbonisation, alternative clean fuels for propulsion systems are sought. There is definite advantage in retaining the well-established principles of operation of combustion engines at the core of future developments with hydrogen as a fuel. Hydrogen is envisaged as a clean source of energy for propulsion of heavy and off-road vehicles, as well as in marine and construction sectors. A source of concern is the unexplored effect of hydrogen combustion on dilution and degradation of engine lubricants and their additives, and consequently upon tribology of engine contact conjunctions. These potential problems can adversely affect engine efficiency, durability, and operational integrity. Use of different fuels and their method of delivery, produces distinctive combustion characteristics that can affect the energy losses associated with in-cylinder components and their durability. Therefore, detailed predictive analysis should support the developments of such new generation of eco-friendly engines. Different fundamental physics underpin the various aspects of a pertinent detailed analysis. These include thermodynamics of combustion, in-cylinder tribological interactions of contacting surfaces, and blowby of generated gasses. This paper presents such an integrated multi-physics analysis of internal combustion engines with focus on hydrogen as the fuel. Such an in-depth and computationally efficient analysis has not hitherto been reported in the literature. The results show implications for lubricant degradation due to the use of hydrogen in the performance of in-cylinder components and the underlying physical principles.

Keywords

Hydrogen fuel, combustion, thermodynamics, tribology, lubrication, gas blowby

Date received: 14 February 2023; accepted: 30 May 2023

Introduction

Hydrogen-fuelled internal combustion engines are increasingly considered as alternatives to the conventional engines with fossil fuel, particularly for larger road and off-highway vehicles. They are expected to play an important role in the future for various propulsion applications such as in marine, mining, agriculture, construction, haulage, and stationary auxiliary power plants to smooth out often-erratic power outputs from some renewable energy sources. In general, hydrogen is a promising, but challenging fuel for internal combustion engines.¹

The use of hydrogen as a fuel to generate mechanical motion dates back to 1807.¹ In 1820 Reverend W. Cecil published his work, based on vacuum created by burning a mixture of hydrogen and air.² This event occurred well before the mass-manufactured fossil fuel-based Internal Combustion Engines (ICEs). Hydrogen combustion produces higher flame propagation speeds, but with lower ignition energy. Therefore, it can be considered as a desired fuel for combustion.³ However, the use of

hydrogen as fuel entails some issues of concern, mainly associated with the lack of necessary infrastructure to produce and transport it with a minimal carbon footprint. Furthermore, its storage requirement in a safe, reliable, cost effective, practical and convenient manner is also of some concern.^{1,4,5} In addition, combustion of hydrogen in conventional IC systems poses some challenges, including the adverse effects that hydrogen can have on the metallic components such as embrittlement or excessive wear,^{6,7} among other issues. Hydrogen can also cause more rapid degradation of engine lubricant.⁸ As the result, the lifespan of Hydrogen-fuelled Internal

¹Wolfson School of Mechanical, Electrical and Manufacturing Engineering, Loughborough University, Loughborough, Leicestershire, UK

²School of Engineering, University of Central Lancashire, Preston, Lancashire, UK

Corresponding author:

Ramin Rahmani, Wolfson School of Mechanical, Electrical and Manufacturing Engineering, Loughborough University, Ashby Road, Loughborough, Leicestershire LE11 3TU, UK.

Email: R.Rahmani@lboro.ac.uk

Combustion Engines (HICEs) is generally considered to be lower than their conventional hydrocarbon-fuelled counterparts.⁹ The production of non-carbon emissions such as Nitrogen Oxides (NOx) must also be addressed,¹⁰ as combustion of hydrogen produces higher adiabatic temperatures, resulting in elevated combustion temperatures with a higher NOx generation.³ However, it is possible to reduce the NOx emissions to insignificant levels by adopting a leaner combustion strategy and a lower burn velocity.¹ In turn, this approach has adverse implications on the generated power.¹¹ In this regards, use of techniques such as water injection to dual-fuel Compression Ignition (CI) engines to reduce NOx and improve share of hydrogen energy was investigated by Chintala and Subramanian.¹⁰ As Sens et al.¹² suggested, due to the existence of many unknown parameters, particularly in terms of a potential step-change innovative technological solutions in the future, it would be advisable to pursue hydrogen-fuelled powertrains in parallel to Battery Electric Vehicles (BEVs). This is in order to achieve urgent global Carbon Dioxide (CO₂) reduction targets.

A comparative analysis of use of hydrogen, biofuel, and electrical power for sustainable transport was carried out by Shafiei et al.,¹³ who concluded that the use of hydrogen can be beneficial in reducing fuel import and consumer fuel costs, providing that the costs associated with development of the necessary infrastructure and vehicle ownership are also taken into account. As White et al.¹⁴ highlighted more than a decade ago, continuous research into the advancement of HICE fundamentals, reduction of NOx (without compromising on generated power) and development of advanced engine components are considered as the main challenges, which are still present.

Zero- or one-dimensional (0D/1D) thermodynamic models have been developed to study various thermodynamic and heat transfer aspects of conventional fossil fuel-based ICEs.^{15–18} Such models have also been adapted to study HICEs, for example by Karagoz et al.¹⁹ who investigated the performance of a hydrogen-fuelled Spark Ignition (SI) engines and the associated emissions. Their simulations showed that the use of hydrogen as a fuel improved the Brake Thermal Efficiency (BTE) at different engine speeds. However, the actual brake power decreased. They also noted that through an extremely lean combustion process with air-fuel ratios around twice the stoichiometric air-fuel ratio (or Fuel to Air Equivalence Ratio, or FAER, of less than or near 0.6²⁰) for hydrogen, it was possible to achieve considerable reductions in the generated NOx emissions. Therefore, one of the main conundrums in the context of HICEs is the contradictory requirements between desired gain in maximum power and a reduction in NOx emissions. Under stoichiometric operating conditions and assuming constant volumetric efficiency and thermal losses, switching the fuel from gasoline to hydrogen can result in 17% reduction in output power according to Rana et al.²⁰

Thermal efficiency of HICEs can be 55.6% higher than for a gasoline engine (38.9% with hydrogen against 25% with gasoline), while the power output of HICE can reach 80% that of a gasoline-fuelled counterpart under laboratory conditions.²¹

The performance of engines using hydrogen as an assistive fuel has also been investigated. For instance, Mathai et al.⁸ investigated the differences in performance achieved through use of pure Compressed Natural Gas (CNG) and CNG combined with 18% hydrogen (HCNG) in Spark Ignition (SI) engines under relatively long duration testing (60 h). They noted that the iron deposits on the spark plugs, and cylinder liners was higher for the HCNG engines. In addition, kinematic viscosity, and Total Base Number (TBN) values for the lubricant (15W40) was significantly lowered with the use of HCNG (a drop of 1.3% in the kinematic viscosity and 15% in Total Acid Number or TAN). Subsequently, higher concentration of wear metallic partners such as iron and copper were also detected when using oil from HCNG. One of the main issues with the use of hydrogen as supplementary fuel to gasoline or diesel is the reduction in the volumetric efficiency due to the lower heating value of hydrogen, which results in lower torque and output power.³ It also reduces BTE due to a reduction in combustion efficiency because of the addition of hydrogen. Adding hydrogen as a supplementary fuel to diesel-fuelled Compression Ignition (CI) engines increases the Brake-Specific Fuel Consumption (BSFC) but reduces the formation of soot.³ Usman et al.²² have also investigated the use of different fuels in an ICE including gasoline, CNG, and CNG and hydroxy gas (HHO) in 120 h engine tests. CNG-HHO blend resulted in significant effect upon lubricant viscosity, flash point and TBN mainly due to the addition of water as the result of combustion (5% after 40 h high loading conditions). This fuel also increased the various metallic wear particles. Furthermore, the reduction in Zn additives was higher for the CNG-HHO fuel (14.2%) in line with findings of Verhelst and Sierens²³ and Yildiz and Ceper²⁴ who used a zero-dimensional single zone SI engine thermodynamic model to study the effect of methane and methane-hydrogen blend. They found that the use of fitted double-Wiebe function provides better results for combustion modelling of these fuels.

Lubricants must also be compatible with the surge in water concentration in the crankcase,¹ with hydrogen combustion. This points to the potential use of either a demulsifying lubricant or a synthetic lubricant, which can form a solution with water.²⁵ The experimental investigation of Verhelst and Sierens²³ with a SI HICE showed that the properties of engine oil were significantly affected in terms of their quality. The concentration of various additives such as zincdialkyldithiophosphate (ZDDP), used as an anti-wear inhibitor was greatly decreased along with almost complete disappearance of esters, which can be explained as the ability of hydrogen in breaking down the double carbon – carbon bonds.

Additionally, viscosity of the oil increased at cooler temperatures, whilst it was reduced rapidly at the higher operating temperatures. The viscosity index of the used oil was 99, which was considerably lower than that of the fresh lubricant at 163.

An interesting investigation on the effect of hydrogen on piston ring wear was conducted by Kindrachuk et al.²⁶ They proposed that hydrogen can be generated because of the breakdown or decomposition of lubricants in temperatures and pressures experienced inside the combustion chamber. This, in turn, can cause diffusion of hydrogen into the solid material structure mainly due to the energy provided through sliding friction. The tribological effect of the use of Modified Microalgae Oil (MMO) as a bio-lubricant for hydrogen powered ICE was investigated by Cheah et al.,²⁷ in which they found that there could be around 10% reduction in the coefficient of friction through use of MMO. However, issues such as high acidity of the MMO should also be addressed.

An important aspect related to HICEs which remains insufficiently explored is the implication of hydrogen combustion on the tribological performance of in-cylinder components. There is indication that the current lubricant formulations should be altered in order to better serve HICEs in reducing their relatively rapid degradation.^{23,28} It is shown that the conditions of the in-cylinder components can significantly affect the generated contact pressures and temperatures during the combustion process.^{29,30} Therefore, an in-depth tribological investigations cannot be carried out in isolation from the combustion process itself. There are also some, albeit relatively minor, counteracting effects from in-cylinder tribology on thermodynamics of the combustion process based on the loss of useful work due to friction as well as loss of in-cylinder charge due to blowby. Blowby of hydrogen from cylinder can be quite high due to the rapid pressure rise as a result of a faster burn rate and the lower density of hydrogen.²³ Therefore, a hydrogen ventilation system is required to keep safe levels (< 1% vol) in the crank case.¹ These issues point to the need for developing coupled thermodynamic and tribological analysis/predictive models.

Considering the complexities involved in detailed thermodynamic analysis of the combustion process, achieved mainly through CFD,³¹ and development of detailed multiscale in-cylinder tribological models,^{32,33} a fully numerical and detailed coupled model can be very time consuming from the computational perspective. This can also prevent wider use of such tools in industry as practical holistic analysis tools for engine designers. Therefore, developing combined multi-physics analytical models, which require lesser computational time, but provide sufficiently accurate results as presented in this study, seems to be the appropriate approach. Therefore, the aim of the current study is to develop an analytical model, combining thermodynamics of combustion with an in-cylinder tribology. To achieve this aim, a zero-dimensional thermodynamic model is

developed and coupled with an analytical model for tribology of piston rings, including gas blowby. The approach expounded here utilises the existing models used for conventional engines and adapts those for the case of hydrogen-fuelled engines wherever the relevant data or relationships are available. This approach is original and has not hitherto been reported in the open literature, particularly in the context of conventional IC engines or indeed for the hydrogen-fuelled alternatives. Furthermore, the approach presented in the current study paves the way for more refined and complex model for analysis of IC engines in the future.

Analytical modelling approach

Thermodynamic model

The analytical approach for modelling the combustion process takes into account a zero-dimensional (0D) model, based on the first law of thermodynamics. For the system of concern, the first law of thermodynamics can be stated as:

$$\dot{E} = (\dot{Q}_c - \dot{Q}_l) + (\dot{W}_f - \dot{W}_p) + \left(\sum \dot{m}_i h_i - \sum \dot{m}_o h_o \right) \quad (1)$$

If the contributions from the gravitational potential and kinetic energies of gases is neglected, the total energy, E , equates the internal energy of the system, U , thus:

$$E = U = mc_v T \quad (2)$$

In addition, the rate of release of heat, \dot{Q}_c , through combustion is obtained as:

$$\dot{Q}_c = \eta_c m_f \dot{x}_b Q_{LHV} \quad (3)$$

where, η_c is the combustion efficiency, m_f is the mass of fuel, \dot{x}_b is the burn rate of the fuel, and Q_{LHV} is the lower heating value of the fuel.

The initial mass of the in-cylinder charge is determined, using the ideal gas law as:

$$m = \frac{P_0 V_0}{R_s T_0} \quad (4)$$

where, $R_s = R_0/M$ is the specific gas constant, R_0 is the universal gas constant and M is the molar mass of the in-cylinder mixture content. With gasoline as fuel, the initial in-cylinder mass is considered to be the mass of air as fuel droplets occupy a negligible portion of the cylinder volume and their mass can thus be neglected in comparison to that of the trapped air. However, for HICE, the mass of the cylinder content is determined, based on the type of fuel delivery system. For carburetted or Port Fuel Injection (PFI) delivery systems (mixture aspirating operation), the hydrogen can displace a relatively larger volume of the combustion chamber (almost 30% of the total cylinder volume at the stoichiometric air-fuel ratio). Therefore, this leaves less space for the trapped air.^{20,34} Consequently, the

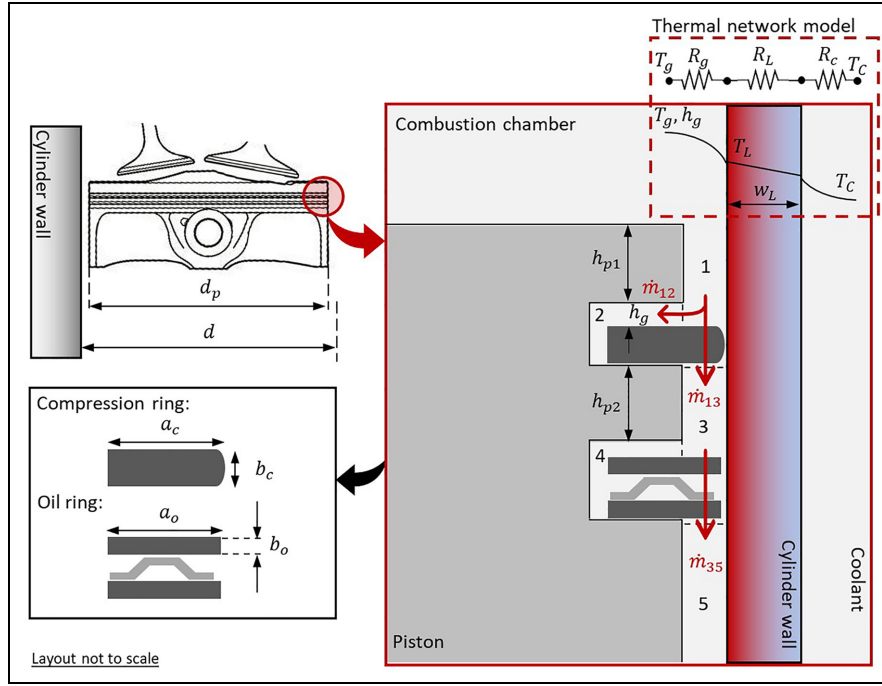


Figure 1. Schematic representation of the combustion chamber and the in-cylinder components including the piston, the top compression ring, and the oil control ring as well as the schematics of the thermal network model and gas blow by directions.

initial mass of the in-cylinder charge can be determined by considering:

$$R_s = \frac{(M_a + AFRM_f)R_0}{M_a M_f (1 + AFR)} \quad (5)$$

from which the in-cylinder fuel and air masses are determined as:

$$m_f = \frac{m}{1 + AFR} \quad (6)$$

$$m_a = \frac{m AFR}{1 + AFR} \quad (7)$$

In Direct Fuel Injection (DFI) systems (air-aspirating operation) the total volume of the cylinder is fully occupied by air at the start of the process, thus: $R_s = R_0/M_a$.

The rate of heat loss through the combustion chamber, \dot{Q}_l , can be determined by taking into account the thermal resistive barriers to the flow of heat from the combustion gas to the coolant jacket, as well as through thermal radiation³⁵:

$$\dot{Q}_l = \frac{A_c(T - T_c)}{\frac{1}{h_{cc}} + \frac{w_l}{k_l} + \frac{1}{h_c}} + \varepsilon \sigma_{SB} A_c (T^4 - T_l^4) \quad (8)$$

where, T_c is the coolant temperature, A_c is the heat transfer area of the combustion chamber, and h_{cc} is the convective heat transfer coefficient of the combustion gases against the cylinder liner wall. w_l and k_l are the liner substrate wall thickness and thermal conductivity of the liner material, whilst h_c is the convective heat transfer coefficient in the coolant side (see Figure 1 for

the schematic representation of the associated thermal network model).

The radiation factor, $\varepsilon_s = 0.075$ for spark ignition engines and the Stefan-Boltzmann constant is $\sigma_{SB} = 5.67 \times 10^{-8} \text{ W/m}^2 \text{ K}^4$.³⁶ Use of this method also allows the determination of average cylinder liner temperature as a function of engine operating conditions.

The rate of irreversible work originated from parasitic frictional losses is equivalent to the frictional power loss in the system, given as:

$$\dot{W}_f = f \dot{s} \quad (9)$$

where, friction, f , is obtained through a tribological analysis of the contacts of concern in an IC engine, particularly those related to the piston ring-pack and cylinder liner contacts and \dot{s} is the piston velocity.

Finally, the rate of work done by the piston is:

$$\dot{W}_p = p \dot{V} \quad (10)$$

where, p and V are the instantaneous cylinder pressure and volume.

The enthalpy of the inlet flow to the system, which is due to injection of the fuel (considering its relatively small amount) can be neglected. Therefore, in the current study it is assumed that: $\dot{m}_i h_i = \dot{m}_f h_f \cong 0$. The enthalpy of the outflow, which is due to combustion gas blowby through the crevices in the piston ring-pack, is also relatively small. However, it is kept in the governing equation as these blowby gases not only affect the thermodynamic efficiency of the engine, but also contribute to the potential adverse environmental pollution. Thus, $\dot{m}_o h_o = \dot{m}_b c_p T$, where \dot{m}_b is the blowby

mass flow rate and is assumed that the specific enthalpy of the blow-by gasses is the same as the enthalpy of the combustion gas.

Considering the ideal gas law, in which the pressure, volume and temperature are considered as functions of the crank-angle, it follows that:

$$p(\theta)V(\theta) = mR_0T(\theta) \quad (11)$$

Substituting equations (2) to (6) into equation (1) along with expressing the rates of changes in terms of crank-angle, it follows that:

$$\frac{dp(\theta)}{d\theta} + \varphi(\theta)p(\theta) = \frac{\gamma(\theta) - 1}{V(\theta)}\psi(\theta) \quad (12)$$

where:

$$\varphi(\theta) = \frac{\gamma(\theta)}{V(\theta)} \frac{dV(\theta)}{d\theta} - \frac{1}{\gamma(\theta) - 1} \frac{d\gamma(\theta)}{d\theta} + \frac{\gamma(\theta)}{\omega} \frac{\dot{m}_b(\theta)}{m} \quad (13)$$

$$\begin{aligned} \psi(\theta) = & \eta_c(\theta)Q_{LHV}m_f \frac{dx_b(\theta)}{d\theta} - \frac{h_c(\theta)A_c(\theta)}{\omega} [T(\theta) - T_w] \\ & + f(\theta) \frac{ds(\theta)}{d\theta} + \frac{\dot{m}_f h_f}{\omega} \end{aligned} \quad (14)$$

Equation (12) is a first order non-homogeneous ordinary non-linear differential equation with variable coefficients. The initial conditions required for its solution can be stated as: $p(\theta_0) = P_0$ and $T(\theta_0) = T_0$, where the pressure and temperature are considered to be known a priori at the starting (initial) crank-angle.

For gasoline fuel, the burn rate can be estimated based on the Wiebe distribution function. Thus, the burn rate for the fuel against the crank-angle becomes:

$$\frac{dx_b(\theta)}{d\theta} = \frac{(n+1)a_w}{\Delta\theta_d} \left(\frac{\theta - \theta_s}{\Delta\theta_d} \right)^n \exp \left[-a \left(\frac{\theta - \theta_s}{\Delta\theta_d} \right)^{n+1} \right] \quad (15)$$

where, θ_s is the crank-angle at which the combustion process is initiated and $\Delta\theta_d$ represents the duration of combustion. The parameters a_w and n , which are termed as Wiebe combustion efficiency and form or shape factors, are normally considered to be 5 and 2 respectively for conventional gasoline engines.³⁵ However, there are no generally agreed burn rate models for hydrogen-fuelled engines. Ma et al.³⁶ calculated the heat release rate, based on Wiebe distribution function for SI HICEs, in which the Wiebe combustion efficiency factor was taken as 6.908. However, the presented data were not validated as outlined by Verhelst and Sierens.³⁷ For a blend of hydrogen-methane fuel, Diaz et al.³⁸ used Wiebe function parameters of 2.8 and 2.4 for combustion efficiency and shape factors, whilst Shivapuji and Dasappa³⁹ found different values for combustion of generated gas. Generally, a double or multiple Wiebe function is recommended for combustion of a mixture of fuels.⁴⁰ Luo and Sun⁴¹ used the normal Wiebe

function parameters to model hydrogen combustion. However, they adapted the model to a Wiebe two-zone combustion model which was also suitable for the prediction of knock characteristics. Maamri et al.⁴² also tried to find empirical relationships between Wiebe parameters and engine specifications. Alam and Depcik⁴³ proposed adaptive Wiebe function parameters for PFI hydrogen-fuelled engines. In their work Wiebe function values of 5 and 1.5, for combustion efficiency and shape factor were used for combustion of hydrogen.⁴⁴ This was regarded as high hydrogen flame propagation, being six-fold and nine-fold faster than that for gasoline or methane and diesel.^{1,3}

The heat transfer coefficient within the combustion chamber can be obtained using the well-known relationship provided by Woschni,⁴⁵ amongst other suggested and widely used relationships.⁴⁶⁻⁴⁸ However, all these models have been developed for conventional ICEs. Demuynck et al.⁴⁹ investigated the compatibility of such models for HICEs and concluded that they cannot adequately describe the heat transfer accurately. Therefore, some modifications would be required. Some specific or modified heat transfer models for use with HICE's have been proposed.⁵⁰⁻⁵² However, these require some specific inputs, usually involving either experimental measurements or predicting the same through complex detailed numerical analysis. Therefore, to avoid variability in the results due to the uncertainty in such inputs from these proposed models, the relationship in equation (16), provided by Woschni⁴⁵ is used in the current study, similar to its use by Karagoz et al.¹⁹ for HICE, and the same by Namar and Jahanian⁵³ for a Homogenous Charge Compression Ignition (HCCI) engine fuelled by hydrogen³⁵:

$$\begin{aligned} h_{cc}(\theta) = & 0.013d^{-0.2}p(\theta)^{0.8}T(\theta)^{-0.53} \\ & \left\{ C_1u_m + \frac{C_2(V_d + V_c)T_0}{P_0V_0} \left[p(\theta) - P_0 \left(\frac{V_0}{V(\theta)} \right)^{1.33} \right] \right\}^{0.8} \end{aligned} \quad (16)$$

For the compression and power strokes $C_1 = 2.28$ and $C_2 = 0.00324$ respectively, else these constants are set to zero. Furthermore, if N and S represent the engine speed in Revolutions per Minute (RPM) and the stroke length respectively, then the mean piston speed is: $u_m = NS/30$, and P_0 , T_0 , and V_0 are the reference or initial in-cylinder pressure, temperature, and volume (e.g. at the start of the compression stroke). Additionally: $V_d = \pi d^2 S/4$ is the total displaced or swept cylinder volume calculated, based on the cylinder bore diameter and stroke, and $V_c = V_d/(\beta - 1)$ is the clearance (i.e. the minimum) cylinder volume, where β is the compression ratio. The variation of cylinder volume with crank-angle is given as⁵⁴:

$$V(\theta) = V_c + \frac{\pi}{4} d^2 s(\theta) \quad (17)$$

where, the instantaneous piston displacement, measured from the TDC is:

$$s(\theta) = l + r(1 - \cos\theta) - (l^2 - r^2 \sin^2\theta)^{\frac{1}{2}} \quad (18)$$

where, l is the connecting rod length and r is the crank-pin radius.

The heat transfer area in equation (8) can be estimated as:

$$A_c(\theta) = \frac{4}{d} V_c + \pi ds(\theta) \quad (19)$$

Once pressure and temperature for each crank-angle is calculated through solution of equation (12) along with equation (11) (see subsection 2.4 for method of solution), it is possible to determine the engine performance parameters of interest.

Using a thermal network model presented in Figure 1, the average liner temperature is approximately given as:

$$T_l = T_c + \frac{\omega \int \dot{Q}_l d\theta}{2\pi A_l} \left(\frac{w_l}{k_l} + \frac{1}{h_c} \right) \quad (20)$$

The liner temperature varies along the piston stroke in IC engines.⁵⁵ Therefore, a variable liner temperature can potentially provide a more accurate set of results, when the tribology of piston ring and cylinder contact is of interest.²⁹

Engine performance parameters of interest include the Indicated Mean Effective Pressure (IMEP), as well as Friction Mean Effective Pressure (FMEP):

$$\text{IMEP} = \int p dV \quad (21)$$

$$\text{FMEP} = \int W_f d\theta \quad (22)$$

Brake Mean Effective Pressure (BMEP) can be calculated by subtracting FMEP from IMEP and the indicated specific fuel consumption. Furthermore, brake thermal efficiency, η_{th} , is obtained by dividing brake work by the amount of heat released to the system, Q_c .

Tribological model

There are three main contributors to the in-cylinder friction in an engine. These include the Top Compression Ring (TCR), a three-piece Oil Control Ring (OCR) and the piston skirt. Developing a detailed numerical tribodynamics model for each component requires substantial detail as reported in Morris et al.⁵⁵, Turnbull et al.⁵⁶ Combining these numerical models with the developed thermodynamic model would require significant computational power and time, which is beyond the aim of the current study. However, it is appropriate to develop reduced detailed, but realistic and representative tribological models using analytical approaches, particularly for the case of the piston rings which contribute the largest portion of in-cylinder frictional losses. In particular, the top compression ring, acting to seal

the combustion chamber contributes the most to frictional losses and is considered as one of the main causes of failures of the in-cylinder components. Therefore, detailed analytical model for the piston rings is presented in the current study.

Piston rings experience a broad range of regimes of lubrication from hydrodynamics to mixed lubrication and onto direct boundary interactions. Therefore, in the current study, for predictive analysis a method developed by Gore et al.⁵⁷ for analytical evaluation of friction in mixed regime of lubrication for sliding contacts is combined with a hydrodynamic model developed by Rahmani and Rahnejat.⁵⁸

To determine contact friction, it is essential to determine the lubricant film thickness. The hydrodynamic load carrying capacity of a circular ring with a parabolic face-width profile is given as⁵⁸:

$$W_h = \frac{3}{8} \pi \eta_e v_p d \left(\frac{b}{h_0} \right)^2 \frac{1}{\xi^2 \sqrt{\xi-1}} \left\{ \bar{c} \xi^2 [12\bar{c}^2(\xi-1)-1] \left[\tan^{-1}(2\bar{c}\sqrt{\xi-1}) + \tan^{-1}(\sqrt{\xi-1}) \right] + \sqrt{\xi-1}(2\bar{c}+1) [6\bar{c}^2\xi^2 - 2\bar{c}^2\xi - 4\bar{c}^2 + \bar{c}\xi - \xi + 1] \right\} \quad (23)$$

where, the piston sliding speed is given as⁵⁶:

$$v_p(\theta) = r\omega \sin\theta \left\{ 1 + \cos\theta \left[\left(\frac{l}{r} \right)^2 - \sin^2\theta \right]^{\frac{1}{2}} \right\} \quad (24)$$

in which, r and l are the crank-pin radius and the connecting rod length. b is the ring contact face-width, h_0 is the minimum film thickness, and ξ is the ring crown height ratio defined as⁵⁸:

$$\xi = 1 + \frac{h_r}{h_0} \quad (25)$$

Also, $\bar{c} = c/b$, in equation (23), where $\bar{c} \in [0, 1/2]$ is the locus of the cavitation inception point measured from the centre of the contact. For $\xi \in (1, 500)$, \bar{c} can be approximated as:

$$\bar{c} \cong 0.24636\xi^{-0.5062} \quad (26)$$

In addition, the effective viscosity of lubricant at the operating temperature can be evaluated using Vogel–Fulcher–Tammann relationship, widely known as the Vogel's relationship⁵⁹:

$$\eta_e = \eta_0 \exp\left(\frac{\beta_0}{T - T_{vp}}\right) \quad (27)$$

The empirical constants η_0 , β_0 and T_{vp} are evaluated, by curve-fitting the Vogel's relationship with measured lubricant viscosity data for at least three temperatures.⁶⁰ The method is applicable to both fresh and degraded lubricants as long as measured data are available.

The load share of surface asperities is determined as⁵⁷:

$$\frac{|F - W_h - W_a|}{F} < 10^{-3} \quad (32)$$

Once the minimum film thickness is determined, the viscous friction is obtained as:

$$f_v = \frac{\pi}{4} \eta_e v_p d \left(\frac{b}{h_0} \right) \frac{1}{\xi \sqrt{\xi - 1}} \left\{ -3\xi \left[\bar{c}^2 (\xi - 1) - \frac{1}{4} \right] \tan^{-1} \left(2\bar{c} \sqrt{\xi - 1} \right) + \xi \left[-3\bar{c}^2 (\xi - 1) + \bar{U} + \frac{3}{4} \right] \tan^{-1} \left(\sqrt{\xi - 1} \right) - 3 \left(c + \frac{1}{2} \right) \left[\bar{c} (\xi - 1) + \frac{1}{2} \right] \sqrt{\xi - 1} \right\} \quad (33)$$

The contribution of asperity peaks' interactions to generated friction in mixed and boundary regimes of lubrication is determined through⁶⁰:

$$W_a = \frac{16\sqrt{2}}{15} \pi (\zeta \kappa \sigma)^2 \sqrt{\frac{\sigma}{\kappa}} E^* b \sqrt{2\sigma R} \left\{ \frac{2\sqrt{\lambda}}{3465} [\lambda (\lambda M - 1244.628) + 2136.8655] \right\}_{\lambda_0}^{\lambda_c} \quad (34)$$

where, τ_0 is the characteristic shear stress of the lubricant, ς is the coefficient of boundary shear strength of the asperity tip-pair interactions, which is determined for different lubricant-surface combinations through use of Atomic Force Microscope (AFM) in Lateral Force Microscopy mode (LFM).^{32,62} Therefore, specific values of this parameter can be used in the model if the data for a particular ring or liner surface including the effect of material degradation or formed/affected tribofilms are determined through use of LFM. A_a is the total asperity area of contact⁵⁷:

$$A_a = \pi^2 (\zeta \kappa \sigma)^2 b \sqrt{2\sigma R} \int_{\lambda_0}^{\lambda_e} \frac{F_2(\lambda)}{\sqrt{\lambda}} d\lambda \quad (35)$$

where, $\lambda_e = h_e/\sigma$, in which $h_e = h_0 + b^2/(8R)$ is the gap at the edge of the ring, measured from the surface of the liner. The statistical height distribution function is:

$$F_2(\lambda) = \frac{1}{\sqrt{2\pi}} \int_{\lambda}^{\infty} (\alpha - \lambda)^2 \exp\left(-\frac{\alpha^2}{2}\right) d\alpha = -\frac{1}{4} \sqrt{\frac{2}{\pi}} \left\{ 2\lambda \exp\left(-\frac{\lambda^2}{2}\right) + \sqrt{2\pi} (1 + \lambda^2) \left[\operatorname{erf}\left(\frac{\lambda}{\sqrt{2}}\right) - 1 \right] \right\} \quad (36)$$

Thus, the total friction becomes:

$$f = f_v + f_b \quad (37)$$

Consequently, the power loss or the rate of loss of work by the top compression ring (TCR) is obtained as:

$$\dot{W}_f = f v_p \quad (38)$$

This is subsequently used in calculating work done by friction in the thermodynamic analysis.

A similar approach is applied to both segments of the three-piece oil control ring used in the studied engine. However, in this case, the effect of combustion gas on the applied force on the oil control ring is neglected, indicating that the pressure in the oil ring retaining groove is assumed to be equal to the crank-case pressure.

where, $M = -1.449\lambda^3 + 22.099\lambda^2 - 146.421\lambda + 543.5892$, $\lambda_0 = h_0/\sigma$, and $\lambda_c = h_c/\sigma = \min[2.2239, \lambda_0 + b^2/(8R\sigma)]$, where σ is the composite Root Mean Square roughness (RMS) of the combined ring and liner surfaces. Additionally, λ is the Stribeck oil film thickness ratio, R is the radius of curvature of ring crown, ζ is the density of asperity peaks per unit area, κ is the average radius of curvature of asperity tips, and E^* is the composite Young's modulus of elasticity of the continuous surfaces, determined as:

$$\frac{1}{E^*} = \frac{1 - \nu_1^2}{E_1} + \frac{1 - \nu_2^2}{E_2} \quad (29)$$

where, the indices 1 and 2 denote the ring and the liner respectively, and ν is Poisson's ratio. It should be noted that use of hydrogen as a fuel can potentially affect the solid material properties through processes such as embrittlement. Therefore, when calculating equivalent modulus of elasticity of the surfaces such effects can be considered subject to availability of material properties for the affected surfaces of the ring or the liner.

The total load applied on the piston ring, F , is due to ring elastic tension and the outward radial force due to combustion gas pressure acting behind the inner rim of the piston ring. The former is a known for a given ring, but the latter varies in the piston cycle, determined through gas-blow analysis (see subsection 2.3).

For instantaneous equilibrium of forces acting on the ring:

$$F = W_h + W_a \quad (30)$$

An iterative solution is used where the initially assumed minimum film thickness value is continuously updated by⁶¹:

$$h_0^k = h_0^{k-1} \left(1 + 0.01 \frac{W_h + W_a - F}{F} \right) \quad (31)$$

Successive iterations are carried out until the following convergence criterion is satisfied:

Combustion gas blow-by

The blowby flow of combustion gases is calculated, based on the methodology provided initially by Namazian and Heywood,⁶³ and applied by Baker et al.⁶⁴ and Turnbull et al.⁵⁶ to piston ring-packs similar to the engine subject of the current analysis. Figure 1 provides schematic representation of the blow-by flow components employed for the studied engine.

A major source of gas blowby is through the incomplete circular compression ring's end-gap. The mass flow rate through the end-gap is calculated, based on the flow of gas through an orifice as:

$$\dot{m}_{ij} = C_d A_{ij} \rho_i c_i \eta_{ij}, \quad (i = 1, j = 3 \text{ or } i = 3, j = 5) \quad (39)$$

where, A_{ij} is the area orthogonal to the direction of gas flow, and ρ_i and $c_i = \sqrt{\gamma P_i / \rho_i}$ are the density of gas and the speed of sound in a region at pressure P_i , which is assumed to be the same as the in-cylinder pressure for TCR and the inter-ring pressure for OCR. C_d is the gas discharge coefficient:

$$C_d = 0.85 - 0.25 \left(\frac{P_j}{P_i} \right)^2 \quad (40)$$

and the compressibility factor is determined as 73:

$$\eta_{ij} = \begin{cases} \sqrt{\gamma} \left(\frac{2}{\gamma+1} \right)^{\frac{\gamma+1}{2(\gamma-1)}} \text{ if } \frac{P_j}{P_i} \leq \left(\frac{2}{\gamma+1} \right)^{\frac{\gamma}{\gamma-1}} \\ \sqrt{\frac{2\gamma}{\gamma-1} \left(\frac{P_j}{P_i} \right)^{\frac{2}{\gamma}} - \left(\frac{P_j}{P_i} \right)^{\frac{\gamma+1}{\gamma}}} \text{ if } \frac{P_j}{P_i} > \left(\frac{2}{\gamma+1} \right)^{\frac{\gamma}{\gamma-1}} \end{cases} \quad (41)$$

Depending on the balance of forces acting on the piston ring, it can translate axially inside its retaining piston groove. The resultant force on the ring is:

$$F_r(\theta) = F_p(\theta) + F_f(\theta) + F_g + F_i(\theta) + F_s(\theta) \quad (42)$$

where, $F_p(\theta)$ is the force due to gas pressure, given as:

$$F_p(\theta) = \frac{\pi}{2} (P_1 - P_3) \left[\left(\frac{d}{2} \right)^2 - \left(\frac{d}{2} - a_r \right)^2 \right] \quad (43)$$

where, a_r is the radial ring thickness. The force $F_g = m_r g$ is the weight of the ring, where g is the gravitational acceleration. Force $F_s(\theta)$ is the squeeze force which originates from squeezing the lubricant trapped between the ring's annular face and the piston groove lands. In this study, it is assumed that $F_s(\theta) = 0$ in order to reduce from further complexity. The force exerted due to friction is $F_i(\theta) = -|f(\theta)|$ and $F_i(\theta)$ is the force due to ring inertia in its axial oscillations:

$$F_i(\theta) = -m_r \omega^2 \left[\cos \theta + \frac{r^3 \sin^4 \theta + r^2 (\cos^2 \theta - \sin^2 \theta)}{(\rho^2 - r^2 \sin^2 \theta)^{\frac{3}{2}}} \right] \quad (44)$$

Thus, depending on the sign of the net force, the mass flow rate from volumetric region 1 to 2 or from 2 to 3 (Figure 1) can be determined by⁶³:

$$\begin{cases} \dot{m}_{12} = \frac{A_{12} h_g^2}{24a} \frac{P_1^2 - P_2^2}{\eta_g R_0 T_2}, & \text{if } F_r(\theta) > 0 \\ \dot{m}_{23} = \frac{A_{23} h_g^2}{24a} \frac{P_2^2 - P_3^2}{\eta_g R_0 T_3}, & \text{if } F_r(\theta) < 0 \end{cases} \quad (45)$$

where, the viscosity of the blow-by gases is considered to be a function of the piston temperature, thus: $\eta_g = 3.3 \times 10^{-7} T_p^{0.7}$. In equation (45), A_{12} and A_{23} are the crevice areas through which the gas flows, h_g is the gap between the ring and its retaining piston grooves in the axial direction. If the expressed condition for each equation in (45) is not satisfied, then the corresponding mass flow rate diminishes.

As already mentioned, pressure in the region 1 is considered to be the same as the in-cylinder pressure. The pressure in the region 5 is assumed to be the same as the crank-case pressure. However, to determine the pressure in regions 2 and 3, an iterative method of solution should be used (see subsection 2.4). Thus, the pressure in the regions 2 and 3 are updated as⁶³:

$$P_2^k = P_2^{k-1} + \frac{\Delta t}{m_2} (\dot{m}_{12} - \dot{m}_{23}) P_2^{k-1} \quad (46)$$

and,

$$P_3^k = P_3^{k-1} + \frac{\Delta t}{m_3} (\dot{m}_{13} + \dot{m}_{23} - \dot{m}_{35}) P_3^{k-1} \quad (47)$$

where, t is the computational time step. Due to the existence of tension in the springs between the OCR segments, the pressure behind the oil control ring is considered to be the average of pressures in the regions 3 and 5. The mass of the momentarily trapped gas in the regions 1, 2 and 3 can be determined using the ideal gas law. The calculated blowby mass flow rate can then be fed back into equation (12).

Method of solution

For a naturally aspirated engine, pressure and temperature at the onset of the compression stroke, P_0 and T_0 can be set to the ambient atmospheric conditions. This will allow the determination of the mass of intake air. The pressure at the next crank-angle can be obtained based on first order backward finite difference discretisation of the pressure gradient in equation (12) as:

$$\frac{dp}{d\theta} = \frac{p(\theta) - p(\theta - 1)}{\Delta\theta} \quad (48)$$

Therefore, the pressure at the next immediate crank-angle becomes:

$$p(\theta) = \frac{p(\theta - 1) + \Delta\theta \frac{\gamma(\theta)-1}{V(\theta)} \psi(\theta)}{1 + \Delta\theta \phi(\theta)} \quad (49)$$

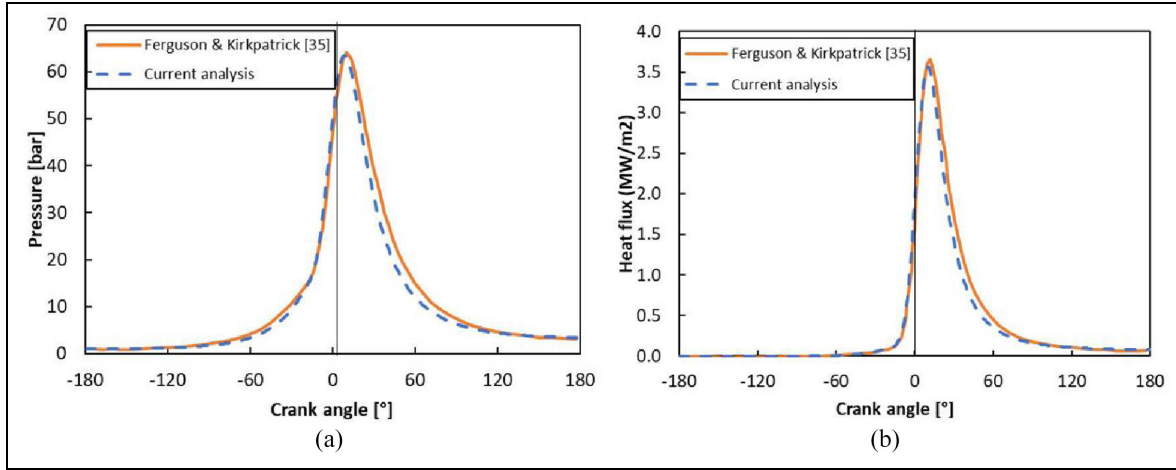


Figure 2. Comparison of: (a) in-cylinder pressure and (b) heat flux values.

Once the pressure is found for all the crank-angles, the temperature is updated using the ideal gas law (equation (11)). The new pressures are then calculated for the entire engine cycle until the difference between the pressures in two consecutive cycles, k and $k - 1$ satisfy the following convergence criterion:

$$\frac{\sum_{i=1}^I |p^k - p^{k-1}|}{\sum_{i=1}^I |p^{k-1}|} < 10^{-6} \quad (50)$$

The crank-angle steps required to achieve converged solution was found to be in the order of 10^{-4} rad. At each crank-angle step the subroutines associated with tribological computations and gas blowby are invoked in order to calculate the corresponding values and feed these back into equation (12).

For the tribological aspects, at each crank-angle step the piston ring operating conditions such as gas pressure behind the rings and the operating temperature are obtained from the combustion and gas blowby models in order to calculate the lubricant film thickness through quasi-static iterations, based on instantaneous equilibrium. The computational convergence for the rings-liner contacts is deemed as achieved when the condition stated in equation (32) is fulfilled. Subsequently, frictional work and power losses are evaluated. Further details on the solution method can be found in.⁵⁷ A flowchart of the simulation procedure is provided in Appendix A.

Model validation

The developed thermodynamic model is validated using the data available in the literature, as well as the data measured from a single cylinder Honda CRF450R high performance motocross motorbike engine. Table 1 lists the input data which is used to validate the results from the developed model, together with those reported by Ferguson and Kirkpatrick.³⁵ For comparison purposes, the cylinder liner temperature was considered to remain

Table 1. Engine data from Ferguson and Kirkpatrick.³⁵

Parameter	Symbol	Value	Unit
Cylinder bore diameter	d	100	Mm
Engine stroke	S	100	Mm
Connecting rod length	l	120	Mm
Compression ratio	β	10	—
Specific heat ratio	γ	1.3	—
Combustion heat	Q_{in}	1764	J
Crank shaft rotational speed	ω	200	rad.s ⁻¹
Combustion commencement angle	θ_s	-20	°
Combustion duration	$\Delta\theta_d$	40	°
Clearance volume	V_c	0.873	Cc
Ambient temperature	T_0	300	K
Cylinder wall temperature	T_w	360	K
Ambient pressure	P_0	1	Bar

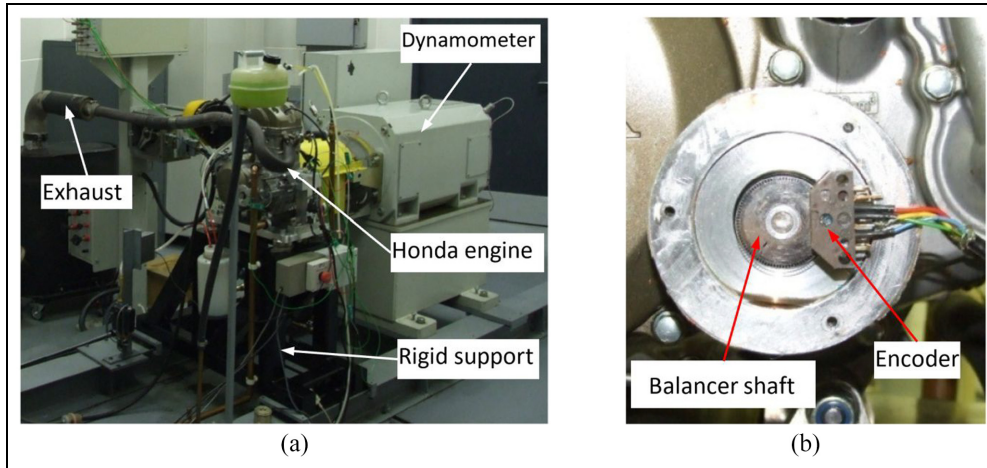
unaltered. In addition, radiation heat transfer, as well as the lost work due to friction generated by in-cylinder components were excluded, a similar approach to that in the original reference.³⁵

The results for in-cylinder pressure against crank-angle are shown in Figure 2. In addition, the engine performance parameters are also compared with those reported in³⁵ in Table 2. As the comparison of the data in Figure 2 and Table 2 show, there is a very good agreement between the current predictions and those in.³⁵ There is only a slight difference in the reported heat losses. This may be due to the marginal differences in the implementation of heat transfer equation or the differences in the type of solvers used.

Post validation of the developed model against the available data from the open literature,³⁵ the predictions from the model are compared with the experimental measurements from a single cylinder naturally aspirated four stroke high performance single cylinder motocross SI Honda CRF 450R engine, mounted on a rigid support structure through a series of anti-vibration neoprene pads. This allows isolation of the engine from its supporting base. The engine gearbox output is aligned and coupled to an Oswald 250 kW

Table 2. Engine data from Ferguson and Kirkpatrick.³⁵

Parameter	Symbol	Current analysis	Verhelst and Sierens ³⁷	Unit	%
Maximum pressure ratio	P_{max}/P_0	63.05	64.22	-	1.82
Normalised net work	W_i/P_0V_0	8.41	8.20	-	2.54
Normalised Heat loss	Q_l/P_0V_0	3.95	4.26	-	7.39
Thermal efficiency	η_{th}	0.42	0.41	-	2.47
Normalised IMEP	$IMEP/P_0$	9.34	9.11	-	2.56

**Figure 3.** (a) Engine dynamometric test setup and (b) an encoder mounted onto the motorbike motocross engine balancer shaft.⁶⁵

transient dynamometer. The dynamometer and engine throttle were controlled by a Ricardo S3000/3345 system (Figure 3(a)). The engine test cell provides a controlled temperature and pressure environment. An OG 90 DN 1024 TTL encoder is utilised to monitor engine speed. A custom-made encoder was mounted to the engine's balancer shaft (Figure 3(b)) to monitor crank and Top Dead Centre (TDC) positions. Cylinder pressure is measured using a spark plug-type Kistler 6081A40 piezoelectric pressure sensor inserted directly into the combustion chamber. All the signals are simultaneously acquired by a LabView software using a National Instrument (NI) BNC-2110 module and NI PCMCIA DAQ (Data Acquisition) card. More details of the engine set up can be found in.⁶⁵ Measurement instrumentation can impose systematic (fixed) and random errors in the measured data due to sensor calibration and unpredictable statistical errors. These errors and the overall uncertainty arising from them for the engine test set-up are reported in⁶⁶ and is provided here in Appendix B. The data was collected over a sufficiently long period of time after an initial running-in period with constant speed in order to ensure that thermal equilibrium in engine components is reached and the cyclic repeatability in the measurements is achieved. For the average in-cylinder pressure of 70 bars, the standard deviation of peak pressure is 3.65 bars over 20 engine cycles. The measured average liner temperature under the stated operating conditions is approximately

Table 3. Engine specifications and running conditions.

Parameter	Symbol	Value	Unit
Cylinder bore diameter	d	96.0	mm
Engine stroke	S	62.1	mm
Connecting rod length	l	107.0	mm
Compression ratio	β	11.5	-
Specific heat ratio	γ	1.34	-
Air molecular weight	M_a	28.97	g.mol^{-1}
Lower heating value of fuel	Q_{LHV}	45	MJ.kg^{-1}
Crank shaft average rotational speed	ω	396.6	rad.s^{-1}
Combustion commencement angle	θ_s	-8 ± 2	$^\circ$
Combustion duration	$\Delta\theta_d$	45	$^\circ$
Clearance volume	V_c	0.428	cc
Ambient temperature	T_0	293.2	K

equals 110°C, with the liner temperature variation of $\pm 7^\circ\text{C}$ at the top and bottom of the cylinder liner.

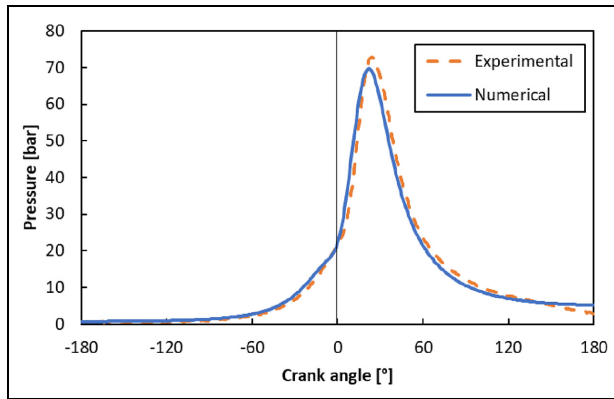
Table 3 lists the engine specifications used for the validation purposes. It should be noted that the exact duration of combustion is not known a priori. Therefore, lining the data for best fit between predictions and measurements is performed through observation.

For predictive analysis, the complete integrated thermodynamic, gas dynamics (blowby) and tribology models are employed. The data in Table 4 lists the input data for the tribological and gas blowby models.

The comparison of the predicted in-cylinder pressure with the measured data is shown in Figure 4. Very good

Table 4. Input data for the gas blow-by and tribology models.

Parameter	Symbol	Value	Unit
Ring and bore material density	ρ	7874	kg.m^{-3}
Ring free end gap	e_g	12.0	mm
5W40 dynamic viscosity @40°C	$\eta_{40^\circ\text{C}}$	76.55	mPa.s
5W40 dynamic viscosity @100°C	$\eta_{100^\circ\text{C}}$	11.62	mPa.s
Ring root mean square roughness	σ_r	0.235	μm
Bore root mean square roughness	σ_l	0.482	μm
Area density of peaks	ξ	2574	mm^{-2}
Mean peak curvature	κ	0.227	μm^{-2}
Top ring face width	b	0.935	mm
Oil ring face width	b_o	0.383	mm
Top ring radial thickness	a	3.075	mm
Oil ring radial thickness	a_o	1.98	mm
Ring crown height	h_r	12.5	μm
Oil ring crown height	h_o	6.5	μm
Piston top land height	h_p	5.35	mm

**Figure 4.** Comparison of measured and predicted in-cylinder pressures for the single cylinder Honda CRF450R motorbike motocross engine.

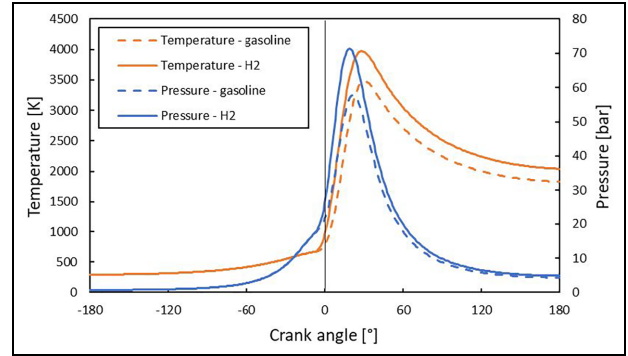
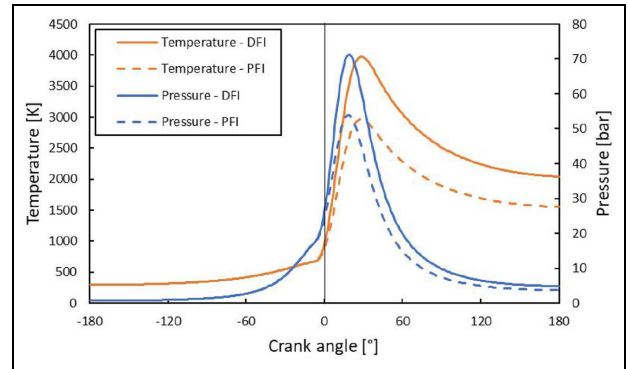
agreement is noted. Therefore, the comparison imparts further confidence in the use of the developed methodology for assessment of the changes in engine performance if hydrogen is used as a fuel.

The tribological models of the piston ring-cylinder liner contact has been validated against measured data from the same engine, reported in Gore et al.⁶⁷ The gas blow-by model is also validated against the work of reported in Namazian and Heywood,⁶³ detailed in Baker et al.⁶⁴

Results and discussion

Effect of fuel and hydrogen delivery method

Figure 5 shows comparison of the results for in-cylinder pressure and temperature for alternatively fuelled hydrogen and gasoline studied engines at their stoichiometric air-fuel ratios. These are 15.03 for gasoline and 34.13 for hydrogen.³⁵ The lower heating value of the hydrogen fuel is 120 MJ/kg.³⁵ Figure 5 shows that at the stoichiometric air-fuel ratio, the generated pressure and temperature for hydrogen fuel is greater

**Figure 5.** Comparison of the predicted in-cylinder pressure and gas temperature with different fuels.**Figure 6.** Comparison of predicted in-cylinder pressures and gas temperature based on different hydrogen fuel delivery systems.

than that of gasoline. Under these stoichiometric conditions, the maximum generated pressure and temperature are 23.11% and 15.35% higher for the hydrogen fuel. As the result, the engine would produce 18.71% more torque and power. This estimate is based on the assumption that the engine would operate with a direct hydrogen fuel injection system. This finding is in line with the expected rise in power density for such a system noted in.¹

With the Direct Injection (DI) configuration, the mass of cylinder content is estimated based on the compressed air only. However, if a carburettor or PFI fuel delivery system is used, where the air and hydrogen are mixed beforehand, then hydrogen would occupy a significant portion of the combustion chamber volume in comparison to the liquid gasoline. Therefore, the performance of stoichiometric air-fuel ratio when hydrogen is used as the fuel is expected to be 86% lower.¹ Figure 6 shows the comparison for in-cylinder pressure and gas temperature when two alternative hydrogen fuel delivery systems are used. The maximum pressure and temperature are 6.97% and 16.08% less than that of the gasoline-fuelled engine, yielding approximately 16% reduction in the engine power, which is in line with the expected drop as noted in.¹ These results imply that although higher power density can be achieved

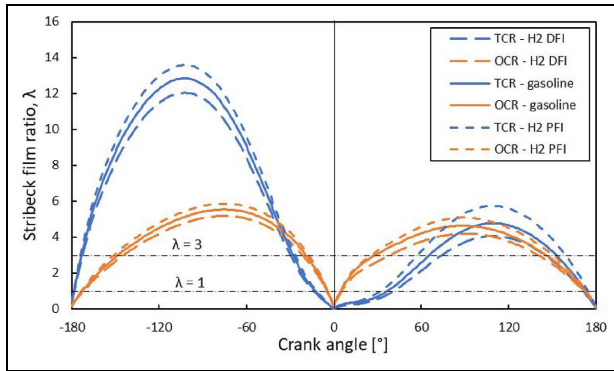


Figure 7. Variations of Stribeck lubricant film ratio for piston rings.

with direct injection due to higher combustion pressures, the generated higher temperatures would potentially produce higher NO_x emissions, particularly that the air-fuel ratio used relates to stoichiometric combustion reaction.

Turning attention to the prediction of tribological performance of hydrogen-fuelled engines, Figure 7 shows the Stribeck oil film ratio, $\lambda = h_0/\sigma$. When $\lambda > 3$, this signifies full fluid film lubrication, whilst when $1 \leq \lambda \leq 3$, the regime of lubrication is mixed and $\lambda < 1$ indicates the prevalence of the boundary lubrication.⁶⁰ Under hydrodynamic regime of lubrication, the viscosity of the lubricant is the most important parameter, determining the tribological contact performance, whilst in boundary regime of lubrication, it is the performance of the lubricant additives such as anti-wear ZDDP and friction modifiers such as Molybdenum Disulphide (MoS₂) becomes important.

Figure 7 shows that during the latter part of the compression stroke and up to around 70° after the TDC for TCR, and up to around crank-angle of 25° past the TDC for the OCR, the regime of lubrication remains mixed. Therefore, the viscous action of the lubricant along with the interaction of opposing asperities on the counter faces determine the overall friction. In the case of the TCR, the regime of lubrication remains boundary up to around the crank-angle of 30° past the TDC. This implies that the contact behaviour in this region is mainly based on the ability of lubricant additives in forming tribo-films. However, in reality, there still would be some contributions from lubricant squeeze film action which can momentarily contribute to the load carrying capacity. This effect is not considered in the current study.

Figure 7 shows that the type of fuel used, and the choice of fuel delivery system directly influence the contact conditions. For instance, it can be seen that the use of DFI can result in harsher tribological conditions through extending the prevalence of mixed and boundary regimes of lubrication in the overall 4-stroke engine cycle.

An important factor which can affect the contact conditions and tribological performance of in-cylinder

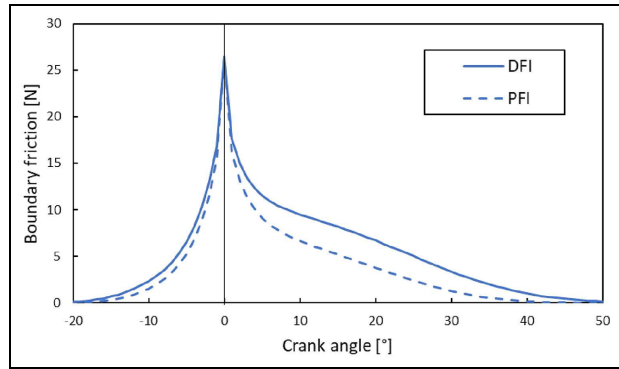


Figure 8. Top compression ring boundary friction contribution in transition from compression to power strokes for hydrogen-fuelled engine.

components is the temperature of the liner. Morris et al.⁵⁵ showed that the lubricant temperature in the piston ring-cylinder liner contact mainly follows that of the liner and only marginally exceeds it. Higher liner temperatures reduce the lubricant viscosity which in turn decreases the contribution due to viscous friction to the overall power loss.²⁹ However, this will increase the probability of enhanced asperity interactions, thus increasing the contribution due to boundary friction. The liner temperature is around 9.83% higher for DFI than PFI, found in the current study (see Figure 11), where it is assumed that the coolant temperature and coefficient of heat transfer remain the same. Therefore, with the DFI system not only the load applied on the ring increases, but also the liner temperature is higher because of an increased combustion temperature. Under these adverse conditions, it is expected that the share of boundary friction would increase. This is shown in Figure 8 for the TCR. As it can be seen, the contribution of boundary friction becomes significant after TDC in the case of a DFI system. At 20° crank-angle the difference is significant, being approximately 77.45%.

The implications of the changes shown in Figures 7 and 8 on the engine performance can be examined, by evaluating the engine performance parameters. Figure 9 shows BMEP and the generated power using hydrogen at different air-fuel ratios and with different fuel delivery systems. The cases for the gasoline fuel are also provided for benchmarking purpose. It is noteworthy that the generated power or BMEP is highest when the engine uses gasoline and runs rich at AFR = 12. The hydrogen fuel is examined at two different air fuel ratios corresponding to stoichiometric and lean burning conditions. The use of hydrogen on DFI system and at stoichiometric AFR provides power which is comparable with the gasoline engine running on rather a rich mixture. With leaner combustion the hydrogen-fuelled engine power tends to reduce. However, these high AFRs are often preferred as they allow mitigation of Nitrogen Oxide (NO_x) emissions at the expense of a drop in power.

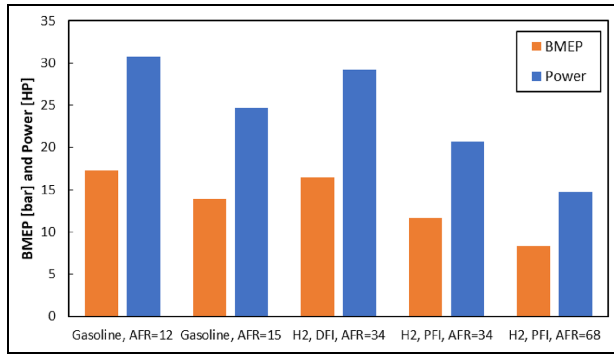


Figure 9. Engine performance parameters based on type of fuel, AFR and fuel delivery system arrangements.

In addition, the BTE and FMEP are shown in Figure 10(a) and (b). The BTE is slightly higher for hydrogen-fuelled engines, particularly if they operate leaner and delivered by a PFI system. The BTE for PFI hydrogen-fuelled engine at equivalence ratio of 2 is around 2.5% higher than that of a gasoline engine at the equivalence ratio of 0.8 as shown in Figure 10(a), whilst the corresponding FMEP is increased by 2.6% (Figure 10(b)). Here it must be noted that the BTE in this study is based on brake power which includes the power lost due to friction from the compression and oil rings for compression and power strokes only and does not include all the other friction losses. Caton⁶⁸ has shown that without including pumping losses and mechanical friction, the BTE values of up to 55% is possible in the thermodynamic simulations.

Temperature of cylinder liner is an important parameter as it determines the effective lubricant viscosity.²⁹ The predicted average liner temperature from the studied case is shown in Figure 11. It is clear that the average liner temperature is higher for DFI hydrogen-fuelled engine than that of the gasoline engine at their stoichiometric air-fuel ratios. The liner temperature drops for hydrogen fuelled engines when they are made to burn leaner to curb NOx emissions.

Figure 12(a) shows the mass flow rate of gas through the piston ring-pack crevices for both gasoline and hydrogen-fuelled engines at their stoichiometric air-fuel ratios with DFI system. With the use of hydrogen, the blowby of gasses tends to be greater. However, it must be noted that in the developed gas dynamics model for hydrogen and with DFI system, properties of air are used throughout the cycle. Part of the gas flow to the back rim of the TCR tends to return to the combustion chamber during latter parts of the power stroke. Therefore, a negative mass flow (back flow) rate is indicated, similar to that reported by Namazian and Heywood for fossil-fuelled engines.⁶³ Comparison of the chosen fuel delivery systems for hydrogen fuel and its effect on blowby gasses is shown in Figure 12(b). It is shown that gas flow rate is higher in the case where a DFI system is used. Under PFI, the combined effect of hydrogen and air is considered when calculating the properties of in-cylinder gases. For a more precise gas dynamic model, the properties of the in-cylinder content after combustion should be included, also taking into account the generated water vapour and the NOx emissions. Based on these results and under both fuel delivery systems, and in particular with DFI, the crank-case ventilation should be considered in the engine design when use of hydrogen as fuel is intended. This is because some of the escaped gases remain with unburnt hydrogen. This action is necessary in order to make sure that volumetric percentage of such unburnt content does not increase to levels which can cause degradation of the engine lubricant in the sump as well as causing any unwanted ignition.¹

Lubrication performance

There is a dearth of quantitative information regarding lubricant degradation for pure hydrogen-fuelled engines. However, there is evidence of the adverse effect of hydrogen on the engine oil, when it is mixed with other fuels such as CNG. As discussed earlier, Mathai

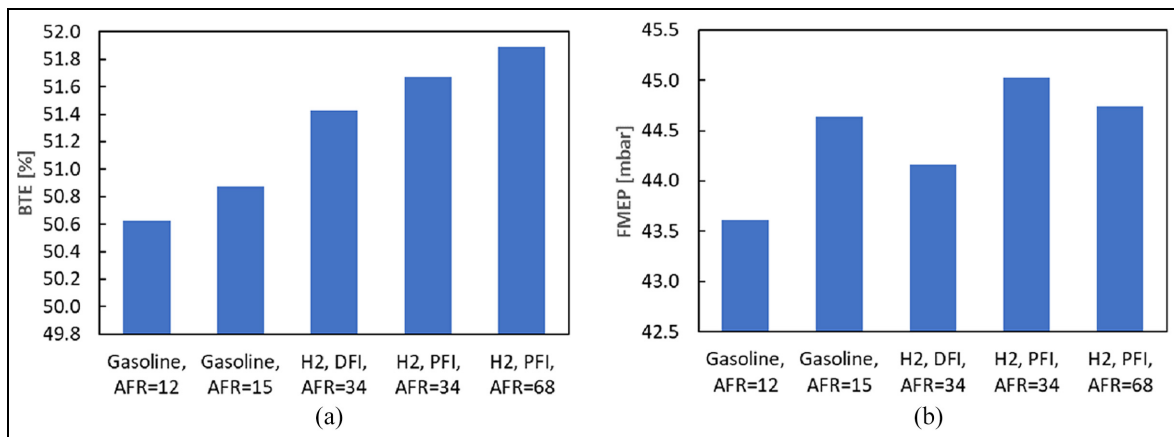


Figure 10. Comparison of: (a) brake thermal efficiency (BTE) and (b) FMEP for different types of fuel, AFR and fuel delivery system arrangements.

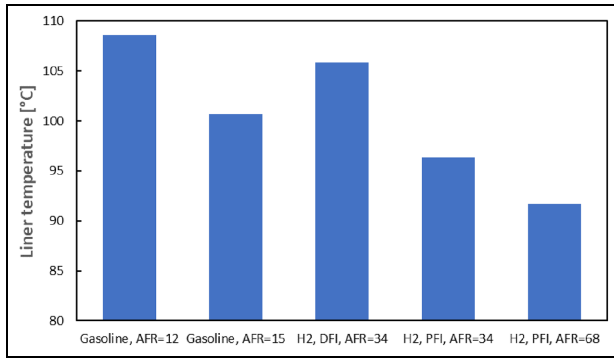


Figure 11. Predicted average liner temperature values.

et al.⁸ showed that 18% hydrogen in CNG can cause oil degradation, including a drop of 15% in lubricant viscosity after 60 h of operation, whilst with CNG alone lubricant degradation was found to be rather negligible. Therefore, the performance of fresh 5W40 lubricant is compared with its degraded alternative with a 15% lower viscosity. The results for the top compression ring are shown in Figure 13. The used oil with reduced viscosity generates less viscous friction as would be expected. However, at the same time the contribution of boundary friction increases with the used oil owing to its reduced load carrying capacity. Nevertheless, overall, the reduction in the viscous friction is higher than the rise in boundary contribution. Based on the calculated FMEP for both TCR and OCR conjunctions, a reduction of 6.43% can be observed. One implication of lubricant degradation is the increase in friction in the parts of engine cycle, where the piston rings experience mixed regime of lubrication as shown in Figure 14(a) and (b).

Figure 14(a) and (b) show the variation in the Stribeck oil film ratio during the power stroke, where the transition from hydrodynamics to mixed regime of lubrication occurs for both TCR and OCR-liner contacts. With lubricant degradation, the contact between TCR and cylinder liner operates under mixed regime of

lubrication for a further 15° crank-angle and in the case of OCR for a further additional 17°. In terms of percentage of engine cycle, these translate to 10.18%. As the result, it is expected that the probability of asperity contacts between the rings and the liner would increase. In the absence or lack of a sufficient volume of lubricant, expected with a degraded oil, severe surface damage to the components and scuffing of the liner surface may occur.

Discussion

It must be noted that the developed modelling approach should be considered as the first step in combined multi-physics analysis of in-cylinder combustion and lubrication study for future clean hydrogen-based engines. The developed model can be further improved by including additional details in thermodynamics, gas blow-by and tribological models. Hydrogen fuel-specific heat release and transfer models may need to be developed and improved further to obtain more accurate predictions. The gas blow-by model must be enhanced to distinguish between the initial cylinder content properties and those that may result post combustion. The tribological model for in-cylinder components can be further improved by including variation of temperature along the liner in piston tribodynamics.^{29,56,61} More detailed piston ring models which would take into account surface roughness effect,⁵⁷ as well as boundary friction properties of the formed tribofilms⁶² should be included in future studies. Utilisation of hydrogen as a fuel can affect the mechanical properties of the solid surfaces in the engine such as the liner and the rings. The proposed tribological model for prediction of mixed and boundary regime of lubrication and associated friction can be used with the inclusion of material properties of degraded surface components to provide more accurate prediction of contact performance for the engine at later stages of their life span. Use of AFM can provide more accurate values for modulus of elasticity and boundary coefficient of shear strength of the in-cylinder components' surfaces^{32,62}

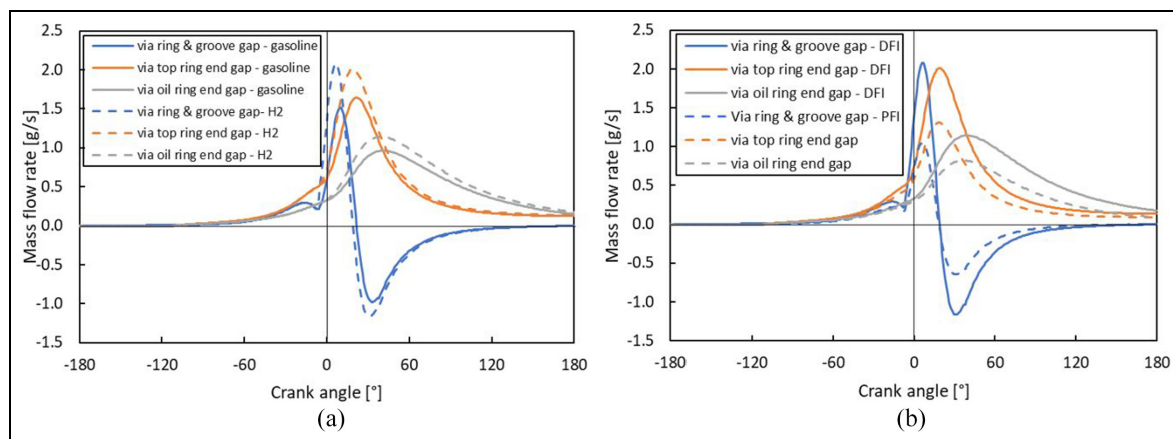


Figure 12. Mass flow rate through piston pack crevices: (a) for gasoline and Hydrogen (H2) fuels and (b) H2 fuel with DFI and PFI system.

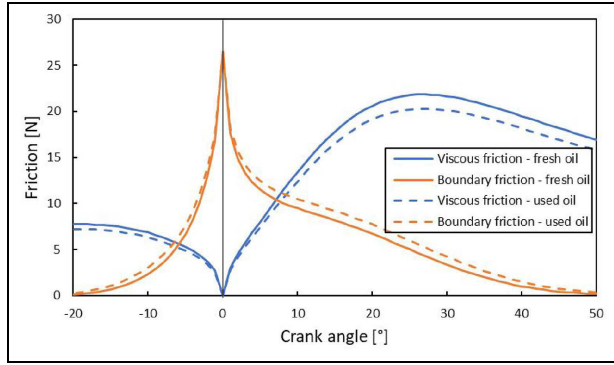


Figure 13. The effect of lubricant viscosity on generated friction in the TCR contact.

which may be subject to degradation or creation of tribofilms.

In addition to changes in lubricant viscosity, covered in the current study, other lubricant physio-chemical attributes can also alter. Oxidation stability of the lubricant can be reduced due to depletion of antioxidants and accumulation of the oxidation products. Water as a hydrogen combustion by-product, not only affects the lubricant viscosity, but also potentially react with the lubricant additives. This can cause breakdown of tribofilms, leading to decreased performance and potential damage to engine. There should be more research for developing lubricants that are specifically formulated to resist the effect of hydrogen, water, and other potential contaminant by-products.

Conclusions

A novel combined analytical thermodynamic, gas blowby and lubrication model is presented to reflect the multiphysics nature of the in-cylinder combustion and tribological performance of hydrogen-fuelled engines. The model is validated against the data available in the open literature³⁵ and further refined, based on the measured data from an actual SI high performance motocross motorbike normally aspirated engine.

Considering the assumptions made in this study, the conclusions of this fundamental study are surmised as:

- Under relevant stoichiometric air-fuel ratios, hydrogen produces higher in-cylinder pressures and temperatures than the fossil fuel counterparts. Hence, higher output power under DFI system is achieved in comparison to a gasoline engine of same capacity. With PFI, the generated pressures and temperatures, and subsequently the engine power, remain somewhat lower.
- The leaner the hydrogen combustion, the ever so slightly higher the thermal efficiency. However, the effect on reduction of power is more pronounced.
- The BTE for the hydrogen-fuelled engine, irrespective of the fuel delivery method is higher than for the gasoline engine at their respective stoichiometric air-fuel ratios.
- The generated volume of in-cylinder blowby gasses from the engine is more for DFI hydrogen-fuelled engine than for the gasoline and PFI hydrogen engine counterparts.
- The liner temperature is lower for leaner combustion of hydrogen and use of PFI. The combustion, and subsequently liner temperature, directly affect the lubricant viscosity. This relationship, as well as combustion pressure acting upon piston ring conjunctions link engine thermodynamics with tribological performance.
- The calculated FMEP, based on the lost mechanical work in piston rings' contacts for DFI hydrogen engine is lower than that for the PFI system even at an air-fuel ratio twice its stoichiometric value. This highlights the importance of viscous friction in determination of FMEP.
- The degraded (used) lubricant with a lower viscosity produces lower FMEP, but it also has a reduced load carrying capacity. Therefore, there are longer periods of direct boundary interactions, with increased boundary friction contribution. Under these circumstances the role of lubricant additives in the formation of low shear strength tribofilms

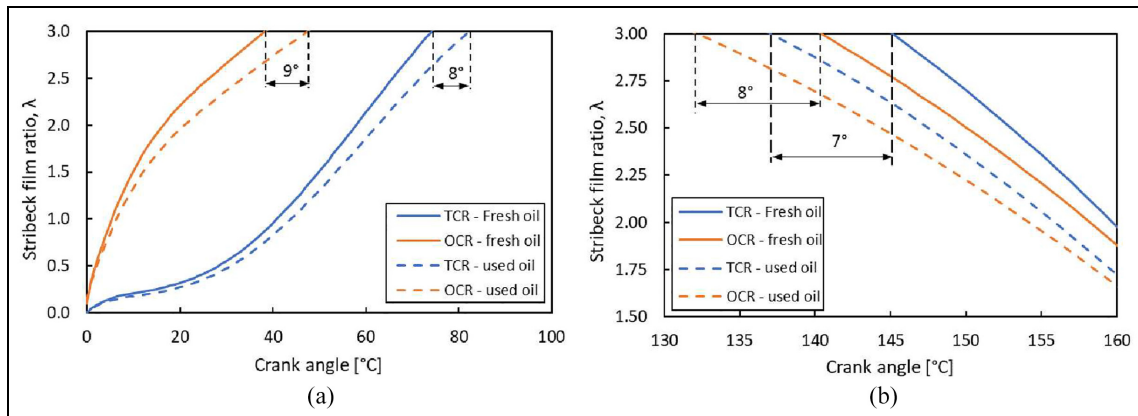


Figure 14. Transition to mixed regime of lubrication in TCR and OCR-liner contacts due to lubricant degradation: (a) 0 to 100 and (b) 130 to 160 degrees of crank angle.

become crucial. Therefore, any degradation or depletion of lubricant additives due to the use of hydrogen becomes an important issue for future investigations.

As discussed earlier, there is a considerable opportunity for developing experimental and numerical techniques, based on multi-physics multiscale approach expounded in this paper for investigation of modern engines particularly those that are to be powered by clean fuels such as hydrogen.


Declaration of conflicting interests


The author(s) declared no potential conflicts of interest with respect to the research, authorship, and/or publication of this article.

Funding

The author(s) disclosed receipt of the following financial support for the research, authorship, and/or publication of this article: The authors gratefully acknowledge the financial support of the Engineering and Physical Sciences Research Council (EPSRC) under the Encyclopaedic program grant (EP/G012334/1), which enabled the development of some of the original gas blowby and in-cylinder tribological models, as well as measurement of experimental engine data used in this study.

ORCID iDs

Ramin Rahmani  <https://orcid.org/0000-0002-6084-8842>

Nader Dolatabadi  <https://orcid.org/0000-0003-3002-1665>

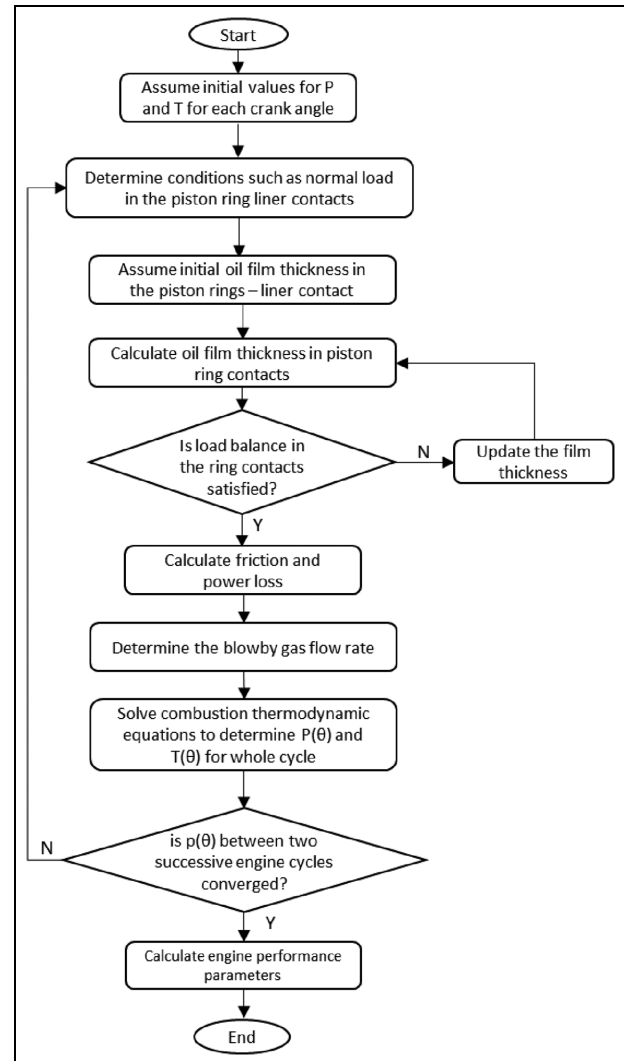
References

- Verhelst S and Wallner T. Hydrogen-fueled internal combustion engines. *Prog Energy Combust Sci* 2009; 35(6): 490–527.
- The Rev. W. Cecil's Engine. Department of Engineering, University of Cambridge, <http://www3.eng.cam.ac.uk/DesignOffice/projects/cecil/engine.html> (2002, Accessed June 2022)
- Shadidi B, Najafi G and Yusaf T. A review of hydrogen as a fuel in internal combustion engines. *Energies* 2021; 14(19): 6209.
- Boretti A. Hydrogen internal combustion engines to 2030. *Int J Hydrog Energy* 2020; 45(43): 23692–23703.
- Hosseini SE and Butler B. An overview of development and challenges in hydrogen powered vehicles. *Int J Green Energy* 2020; 17(1): 13–37.
- Beauregard G. *Findings of Hydrogen Internal Combustion Engine Durability*, Electric Trans. Engineering Corporation, 2010
- Korcek S, Sorab J and Jensen RK. Automotive lubricants for the next millennium. *Indus Lubric Tribol* 2000; 52(5): 209–220.
- Mathai R, Malhotra RK, Subramanian KA and Das LM. Comparative evaluation of performance, emission, lubricant and deposit characteristics of spark ignition engine fueled with CNG and 18% hydrogen-CNG. *Int J Hydrog Energy* 2012; 37(8): 6893–6900.
- Candelaresi D, Valente A, Iribarren D, Dufour J and Spazzafumo G. Comparative life cycle assessment of hydrogen-fuelled passenger cars. *Int J Hydrog Energy* 2021; 46(72): 35961–35973.
- Chintala V and Subramanian KA. Hydrogen energy share improvement along with NO_x (oxides of nitrogen) emission reduction in a hydrogen dual-fuel compression ignition engine using water injection. *Energy Convers Manag* 2014; 83: 249–259.
- Schefer RW, White C and Keller J. Lean hydrogen combustion. In: Derek DR and Peter T (eds) *Lean combustion*. Cambridge: Academic Press, 2008, pp.213–VIII.
- Sens DIM, Danzer IC, von Essen DIC, et al. Hydrogen powertrains in competition to fossil fuel based internal combustion engines battery electric powertrains Wasserstoffantriebe im Wettbewerb mit Verbrennungsmotoren für fossile Kraftstoffe und dem batterieelektrischen Antrieb. In: *42nd International Vienna Motor Symposium*, Vienna, Austria, 2021.
- Shafiei E, Davidsdottir B, Leaver J, Stefansson H and Asgeirsson EI. Energy, economic, and mitigation cost implications of transition toward a carbon-neutral transport sector: A simulation-based comparison between hydrogen and electricity. *J Clean Prod* 2017; 141: 237–247.
- White C, Steeper R and Lutz A. The hydrogen-fueled internal combustion engine: a technical review. *Int J Hydrog Energy* 2006; 31(10): 1292–1305.
- Payri F, Olmeda P, Martín J and García A. A complete 0D thermodynamic predictive model for direct injection diesel engines. *Appl Energy* 2011; 88(12): 4632–4641.
- Fonseca L, Olmeda P, Novella R and Valle RM. Internal combustion engine heat transfer and wall temperature modeling: an overview. *Arch Comput Methods Eng* 2020; 27(5): 1661–1679.
- Mauro S, Şener R, Gül MZ, Lanzafame R, Messina M and Brusca S. Internal combustion engine heat release calculation using single-zone and CFD 3D numerical models. *Int J Energy Environ Eng* 2018; 9(2): 215–226.
- Abu-Nada E, Al-Hinti I, Al-Sarkhi A and Akash B. Effect of piston friction on the performance of SI engine: A new thermodynamic approach. *J Eng Gas Turb Power* 2008; 130(2): 022802.
- Karagöz Y, Balci Ö and Köten H. Investigation of hydrogen usage on combustion characteristics and emissions of a spark ignition engine. *Int J Hydrog Energy* 2019; 44(27): 14243–14256.
- Rana KK, Natarajan S and Jilakara S. Potential of hydrogen fuelled IC engine to achieve the future performance and emission norms. SAE Technical Paper 2015-26-0050, 2015.
- Escalante Soberanis MA and Fernandez AM. A review on the technical adaptations for internal combustion engines to operate with gas/hydrogen mixtures. *Int J Hydrog Energy* 2010; 35(21): 12134–12140.

22. Usman M, Hayat N and Bhutta MMA. SI engine fueled with gasoline, CNG and CNG-HHO blend: comparative evaluation of performance, emission and lubrication oil deterioration. *J Therm Sci* 2021; 30(4): 1199–1211.
23. Verhelst S and Sierens R. Hydrogen engine-specific properties. *Int J Hydrog Energy* 2001; 26(9): 987–990.
24. Yıldız M and Albayrak Çeper B. Zero-dimensional single zone engine modeling of an SI engine fuelled with methane and methane-hydrogen blend using single and double Wiebe Function: A comparative study. *Int J Hydrog Energy* 2017; 42(40): 25756–25765.
25. Project Coordinator Motor Vehicles and Road Transport. TUV Rheinland e.V. For the Federal Ministry for Research and Technology, Alternative energy sources for road transport – hydrogen drive test, Technical report, TUV Rheinland, 1990.
26. Kindrachuk M, Volchenko D, Balitskii A, et al. Wear resistance of spark ignition engine piston rings in hydrogen-containing environments. *Energies* 2021; 14(16): 4801.
27. Cheah MY, Ong HC, Zulkifli NWM, Masjuki HH and Salleh A. Physicochemical and tribological properties of microalgae oil as biolubricant for hydrogen-powered engine. *Int J Hydrog Energy* 2020; 45(42): 22364–22381.
28. Singh S, Bathla VK, Mathai R and Subramanian KA. Development of Dedicated Lubricant for Hydrogen Fuelled Spark Ignition Engine. SAE Technical Paper No. 2019-28-2511, 2019.
29. Rahmani R, Rahnejat H, Fitzsimons B and Dowson D. The effect of cylinder liner operating temperature on frictional loss and engine emissions in piston ring conjunction. *Appl Energy* 2017; 191: 568–581.
30. Ferrarese A, Marques G, Tomanik E, Bruno R and Vata-vuk J. Piston ring tribological challenges on the next generation of flex-fuel engines. *SAE Int J Engines* 2010; 3(2): 85–91.
31. Rakopoulos CD, Kosmadakis GM and Pariotis EG. Evaluation of a combustion model for the simulation of hydrogen spark-ignition engines using a CFD code. *Int J Hydrog Energy* 2010; 35(22): 12545–12560.
32. Styles G, Rahmani R, Rahnejat H and Fitzsimons B. In-cycle and life-time friction transience in piston ring–liner conjunction under mixed regime of lubrication. *Int J Engine Res* 2014; 15(7): 862–876.
33. Turnbull R, Dolatabadi N, Rahmani R and Rahnejat H. Energy loss and emissions of engine compression rings with cylinder deactivation. *Proc IMechE, Part J* 2021; 235(7): 1930–1943.
34. Module 3: Hydrogen use in internal combustion engines. Hydrogen Fuel Cell Engines and Related Technologies, College of the Desert, December 2001, US department of energy, https://www1.eere.energy.gov/hydrogenandfuelcells/tech_validation/pdfs/fcm03r0.pdf (Accessed June 2022).
35. Ferguson CR and Kirkpatrick AT. *Internal combustion engines: applied thermosciences*. Hoboken, NJ: John Wiley & Sons, 2015.
36. Ma J, Su Y, Zhou Y and Zhang Z. Simulation and prediction on the performance of a vehicle's hydrogen engine. *Int J Hydrog Energy* 2003; 28(1): 77–83.
37. Verhelst S and Sierens R. A quasi-dimensional model for the power cycle of a hydrogen-fuelled ICE. *Int J Hydrog Energy* 2007; 32(15): 3545–3554.
38. Diaz GJA, Montoya JPG, Martinez LAC, Olsen DB and Navarro AS. Influence of engine operating conditions on combustion parameters in a spark ignited internal combustion engine fueled with blends of methane and hydrogen. *Energy Convers Manag* 2019; 181: 414–424.
39. Shivapuji AM and Dasappa S. Experiments and zero D modeling studies using specific Wiebe coefficients for producer gas as fuel in spark-ignited engines. *Proc IMechE, Part C: J Mechanical Engineering Science* 2013; 227(3): 504–519.
40. Sapra H, Godjevac M, De Vos P, Van Sluijs W, Linden Y and Visser K. Hydrogen-natural gas combustion in a marine lean-burn SI engine: A comparative analysis of Seiliger and double Wiebe function-based zero-dimensional modelling. *Energy Convers Manag* 2020; 207: 112494.
41. Luo QH and Sun BG. Inducing factors and frequency of combustion knock in hydrogen internal combustion engines. *Int J Hydrog Energy* 2016; 41(36): 16296–16305.
42. Maamri R, Martshenko AP, Osetrov OO, Dubé Y, Toubal L and Kodjo A. Analyze and mathematical modeling of the combustion process of One-Cylinder spark ignited hydrogen fueled engine. *Am J Veh Des* 2013; 1(2): 21–24.
43. Alam SS and Depcik C. Adaptive Wiebe Function Parameters for a Port-Fuel Injected Hydrogen-Fueled Engine. In: *ASME International Mechanical Engineering Congress and Exposition*, November 2019, Vol. 59452: V008T09A015.
44. Babo LFB. *Simulation and Optimization of a Hydrogen Internal Combustion Engine*, PhD Thesis, Universidade DO Porto, Portugal, 2016.
45. Woschni G. A universally applicable equation for the instantaneous heat transfer coefficient in the internal combustion engine. SAE Transactions, 1968, pp.3065–3083.
46. Annand WJD. Heat transfer in the cylinders of reciprocating internal combustion engines. *Proc IMechE* 1963; 177(1): 973–996.
47. Hohenberg G. *Experimentelle Erfassung der Wandwärme von Kolbenmotoren*. Graz: TU Graz, Habil, 1980.
48. Eichelberg G. Some new investigations on Old Combustion engine problems. *Engineering* 1939; 148: 446–463.
49. Demuyneck J, De Paepe M, Huisseune H, Sierens R, Vancollie J and Verhelst S. On the applicability of empirical heat transfer models for hydrogen combustion engines. *Int J Hydrog Energy* 2011; 36(1): 975–984.
50. Demuyneck J, Chana K, De Paepe M and Verhelst S. Evaluation of a flow-field-based heat transfer model for premixed spark-ignition engines on hydrogen. SAE Technical Paper, No. 2013-01-0225, 2013.
51. Michl J, Neumann J, Rottengruber H and Wensing M. Derivation and validation of a heat transfer model in a hydrogen combustion engine. *Appl Therm Eng* 2016; 98: 502–512.
52. Shudo T. A new equation to describe cooling loss in hydrogen combustion engines which was developed from the equation for turbulent heat transfer of pipe flows. *Combust* 2005; 10: 12.

53. Namar MM and Jahanian O. Energy and exergy analysis of a hydrogen-fueled HCCI engine. *J Therm Anal Calorim* 2019; 137(1): 205–215.
54. Heywood JB. *Internal combustion engine fundamentals*. Maidenhead: McGraw-Hill Education, 2018.
55. Morris N, Rahmani R, Rahnejat H, King PD and Fitzsimons B. Tribology of piston compression ring conjunction under transient thermal mixed regime of lubrication. *Tribol Int* 2013; 59: 248–258.
56. Turnbull R, Dolatabadi N, Rahmani R and Rahnejat H. An assessment of gas power leakage and frictional losses from the top compression ring of internal combustion engines. *Tribol Int* 2020; 142: 105991.
57. Gore M, Morris N, Rahmani R, Rahnejat H, King PD and Howell-Smith S. A combined analytical-experimental investigation of friction in cylinder liner inserts under mixed and boundary regimes of lubrication. *Lubric Sci* 2017; 29(5): 293–316.
58. Rahmani R and Rahnejat H. Enhanced performance of optimised partially textured load bearing surfaces. *Tribol Int* 2018; 117: 272–282.
59. Vogel H. Das Temperaturabhaengigkeitsgesetz der Viskosität von Flüssigkeiten. *Physikalische Zeitschrift* 1921; 22: 645.
60. Gohar R and Rahnejat H. *Fundamentals of Tribology*. 3rd ed. Singapore: World Scientific, 2018.
61. Rahmani R, Theodossiades S, Rahnejat H and Fitzsimons B. Transient elastohydrodynamic lubrication of rough new or worn piston compression ring conjunction with an out-of-round cylinder bore. *Proc IMechE, Part J* 2012; 226(4): 284–305.
62. Umer J, Morris N, Leighton M, et al. Asperity level tribological investigation of automotive bore material and coatings. *Tribol Int* 2018; 117: 131–140.
63. Namazian M and Heywood JB. Flow in the piston-cylinder-ring crevices of a spark-ignition engine: Effect on hydrocarbon emissions, efficiency and power. *SAE transactions*, 1982, pp. 261–288.
64. Baker CE, Rahmani R, Karagiannis I, Theodossiades S, Rahnejat H and Frendt A. Effect of compression ring elastodynamics behaviour upon blowby and power loss. *SAE Technical Papers*, Pap. No. 2014-01-1669, 2014.
65. Littlefair B. *A tribo-dynamic solution for the flexible piston skirt and liner conjunction*, PhD Thesis, Loughborough University, Loughborough, UK, 2014.
66. Dolatabadi N, Forder M, Morris N, Rahmani R, Rahnejat H and Howell-Smith S. Influence of advanced cylinder coatings on vehicular fuel economy and emissions in piston compression ring conjunction. *Appl Energy* 2020; 259: 114129.
67. Gore M, Rahmani R, Rahnejat H and King PD. Assessment of friction from compression ring conjunction of a high-performance internal combustion engine: a combined numerical and experimental study. *Proc IMechE, Part C: J Mechanical Engineering Science* 2016; 230(12): 2073–2085.
68. Caton JA. The thermodynamic characteristics of high efficiency, internal-combustion engines. *Energy Convers Manag* 2012; 58: 84–93.

Appendix A: Flowchart of solution methodology



Appendix B: Sources of experimental errors and uncertainties

Table B. Errors and total uncertainty in measured parameters.⁶⁸

Measured parameter	Sensor Manufacturer	Model	Range	Systematic error E_{sys}	Random error Δx_R	Total Uncertainty U_t
Crank angle	Hubner Berlin	TTL 1024	360 pulse/rev	0.03%	0.28%	0.28%
Cylinder pressure	Kistler	6081A40	0–250 bar	0.80%	0.78%	1.12%
Surface Roughness	Alicona	Infinite Focus	0.02–1.19 μm	2.00%	1.60%	2.56%

Appendix

Notation

Roman symbols

A_{12}	crevice area of gas flow from the top to the back of the compression ring	F_r	resultant net force on the top compression ring
A_{13}	crevice area of gas flow through the top compression ring's end-gap	F_s	squeeze film reaction
A_{23}	downward gas flow area from the back of the top ring	f	total friction
A_a	asperity contact area	f_v	viscous friction
A_c	heat transfer surface area of combustion chamber	f_b	boundary friction
A_l	heat transfer area from the cylinder liner	e_p	free ring end-gap
a_w	Wiebe efficiency factor	h_0	minimum lubricant film thickness
a	top ring radial thickness	h_e	lubricant film thickness at the edge of the piston ring
a_o	oil ring radial thickness	h_c	convective heat transfer coefficient in the coolant side
b	top ring face-width	h_{cc}	convective heat transfer coefficient inside the combustion chamber
b_o	oil ring face-width	h_i	specific enthalpy of inlet flow
C_1, C_2	constants in the combustion heat transfer coefficient	h_f	specific enthalpy of fuel
C_d	orifice discharge coefficient	h_g	axial gap between the ring and its retaining groove
c	locus of cavitation inception point (lubricant film rupture)	h_o	specific enthalpy of outlet flow
\bar{c}	dimensionless locus of cavitation inception point	h_{p1}	piston crown height
c_1	speed of sound in the gas above the top piston compression ring	h_{p2}	axial distance between top and bottom piston grooves
c_p	specific heat capacity at constant pressure	h_r	ring crown height
c_v	specific heat capacity at constant volume	k	iteration number
d	cylinder bore diameter	k_l	thermal conductivity of liner material
d_p	piston diameter	l	connecting rod length
E	total system energy	M	intermediate parameter
\dot{E}	rate of change of total system energy	M_a	molar mass of air
E^*	effective modulus of elasticity	M_f	molar mass of fuel
E_1, E_2	modulus of elasticity of ring and liner materials	m	mass of combustion gases
F	total load applied to the piston ring	m_2	mass of gases acting behind the compression ring
$F_2, F_{5/2}$	statistical functions	m_3	mass of gases trapped between the two rings
F_f	friction generated in the top compression ring conjunction	\dot{m}_{12}	mass flow rate from the top of the ring to its rear rim
F_g	weight of the top compression ring	\dot{m}_{13}	mass flow rate through compression ring end-gap
F_i	inertial force of the top compression ring	\dot{m}_{23}	mass flow rate from the back of the ring to the area below the top compression ring
F_p	gas force applied to the top compression ring	\dot{m}_{35}	mass flow rate through the oil ring gap
		\dot{m}_b	mass flow rate of blow-by gases
		m_f	mass of fuel
		\dot{m}_i	mass flow rate into the combustion chamber

\dot{m}_o	mass flow rate out of the combustion chamber
m_r	mass of the ring
N	engine speed in RPM
n	Wiebe form factor
P_0	initial pressure
P_1	gas pressure above the top piston compression ring
P_2	pressure behind the top compression ring
P_3	gas pressure below the top piston compression ring
P_5	crankcase pressure
p	in-cylinder pressure
Q_c	amount of heat released through combustion
\dot{Q}_c	rate of released of heat due to combustion
\dot{Q}_l	rate of heat transfer from the combustion chamber
Q_{LHV}	lower heating value of fuel
R	radius of curvature of piston ring face
R_0	universal gas constant
R_c	thermal resistance between cylinder wall and the coolant
R_g	thermal resistance between combustion gas and liner wall
R_L	liner thermal resistance
R_s	specific gas constant for in-cylinder gases
r	crank-pin radius
S	length of engine stroke
s	piston displacement
\dot{s}	rate of displacement
T, T_g	temperature of combustion gases
T_0	initial temperature
T_2	temperature of the gas behind the top ring
T_3	temperature of the gas in the area below the top ring
T_c	coolant temperature
T_p	temperature of piston
T_w	temperature of cylinder wall
T_{vp}	Vogel's viscosity parameter
t	time
U	internal energy
u_m	piston mean speed
V	instantaneous volume of combustion chamber
\dot{V}	rate of change of volume
V_0	initial (maximum) volume
V_c	clearance (minimum) cylinder volume
V_d	displaced (swept) volume
v_p	piston velocity
W_a	load share of asperity peaks
W_b	brake work
\dot{W}_f	rate of work done by parasitic friction
W_i	indicated work
W_h	hydrodynamic load carrying capacity of piston ring conjunction
\dot{W}_p	rate of work done by piston on combustion gases

\dot{W}_{ps}	rate of work done (power lost) due to piston friction
\dot{W}_r	rate of work done (power lost) due to piston ring friction
w_l	cylinder wall thickness
\dot{x}_b	burn rate of fuel

Greek symbols

α	intermediate integration variable
β	compression ratio
β_0	Vogel's viscosity parameter
γ	specific heat ratio
Δt	time step
$\Delta\theta_d$	duration of combustion in terms of crank-angle
ε	radiation factor
ζ	area density of asperity peaks
η_0	Vogel's viscosity parameter
η_{13}	compressibility factor
η_c	combustion efficiency
η_e	effective dynamic viscosity of lubricant
η_g	dynamic viscosity of gases
η_{th}	thermal efficiency
θ	crank-angle
θ_0	initial crank-angle
θ_s	crank-angle at which combustion commences
κ	average radius of curvature of asperity peaks
λ	Stribeck lubricant film ratio
λ_0	Stribeck lubricant film ratio corresponding to the minimum film thickness
λ_c	critical Stribeck film ratio
λ_e	Stribeck film ratio corresponding to ring edge height
ν_1, ν_2	Poisson's ratios of ring and liner materials
ξ	ring crown height ratio
ρ_1	density of gas above the piston top compression ring end-gap
σ	composite root mean square roughness parameter
σ_{SB}	Stefan-Boltzmann constant
s	coefficient of boundary shear strength of asperities
τ_0	characteristic shear stress of lubricant
φ	intermediate variable
ψ	intermediate variable
ω	angular frequency of crankshaft

Abbreviations

0D/1D	zero or one dimensional
AFM	atomic force microscope
AFR	air-fuel ratio
ICE	internal combustion engine
BEV	battery electric vehicle
BMEP	brake mean effective pressure

BTE	brake thermal efficiency	LFM	lateral force microscopy
CI	compression ignition	MMO	modified microalgae oil
CNG	compressed natural gas	MoS ₂	molybdenum disulphide
CO ₂	carbon dioxide	NO _x	nitrogen oxides
DAQ	data acquisition	OCR	oil control ring
DFI	direct fuel injection	PFI	port fuel injection
DI	direct injection	RMS	root mean square
FAER	fuel-air equivalence ratio	RPM	revolutions per minute
FMEP	friction mean effective pressure	SI	spark ignition
H ₂	hydrogen	TAN	total acid number
HICE	hydrogen-fuelled internal combustion engine	TBN	total base number
HCCI	homogenous charge compression ignition	TCR	top compression ring
HCNG	hydrogen and compressed natural gas	TDC	top dead centre
HHO	Hydroxy gas	ZDDP	zincdialkyldithiophosphate
IMEP	indicated mean effective pressure		